

Hydrogen can both move or pin dislocations in body-centered cubic metals

Received: 26 October 2023

Accepted: 16 April 2025

Published online: 26 April 2025

 Check for updatesKyung-Shik Kim^{1,3}, Qing-Jie Li^{2,3}, Ju Li^{1,2} & Cemal Cem Tasan¹✉

Transition to a hydrogen-based economy requires a thorough understanding of hydrogen interaction with dislocations in metals, especially in body-centered cubic (BCC) steels. Past experimental and computational investigations regarding these interactions often demonstrate two opposing results: hydrogen-induced mobility or hydrogen-induced pinning of dislocations. Through in-situ scanning electron microscopy experiments enabled by a custom-built setup, we address here this discrepancy. Our experiments reveal hydrogen-induced dislocation motion in a BCC metal at room temperature. Interestingly, however, we also observe that the same dislocations are later pinned as well, again induced by the steady hydrogen flux. Molecular dynamics simulations of the phenomena confirm the attraction of the dislocations towards the hydrogen flux, and the pinning that follows after, upon increased hydrogen trapping at the dislocation core. Future experimental or computational studies of hydrogen thus should take into account these different regimes in order to present a full picture of hydrogen defect interactions.

Diffusible hydrogen (H)–dislocation interactions in metals have created significant interest, as well as debates, in the last decades. There are clear experimental and computational demonstrations of both H-induced enhanced dislocation mobility^{1–4}, as well as the opposite effect, i.e., H-pinning of dislocations^{5,6}. An improved understanding of H–dislocation interactions is crucial in the sense that dislocations play major roles in all hydrogen embrittlement (HE) models, i.e., H-enhanced local plasticity (HELP)^{7,8}, H-enhanced decohesion (HEDE)^{9–11}, or H-enhanced void formation (HESIV)^{12,13}. In the case of HELP, for example, H is proposed to facilitate dislocation motion, reduce dislocation interactions, and even to promote dislocation nucleation^{1–4,7,8}. HEDE is mostly attributed to the decrease of the cohesive energy of interfaces and surfaces^{9,10}, but the role of dislocation emission restriction is also proposed¹¹. In HESIV, it is proposed that dislocations can facilitate the transport of V–H clusters, thereby accelerating the aggregation of vacancies and contributing to failure¹³. Enhanced understanding of H–dislocation interactions could help fine-tune all these H-assisted failure models.

Unfortunately, for metals with body-centered cubic (BCC) crystal structure (which includes most steels), unraveling the underlying physics is particularly challenging experimentally, due to the high H

diffusivity, even when dedicated techniques are used^{1–3,6}. To study these challenging interactions here, we employed a home-built in-situ scanning electron microscopy test setup for capturing microstructure evolution. In our approach, H–defect interactions can be captured by electron channeling contrast imaging (ECCI) under well-defined boundary conditions (i.e., without external stress or thin-film effects)^{14,15}. These experiments and the accompanying molecular dynamics simulations enabled us to produce (and explain) the first observations of solely H-induced, external stress-free, dislocation motion in BCC metals. Intriguingly, this approach also revealed that the same dislocations can be pinned by H as well.

The power of this experimental–computational approach was demonstrated earlier for face-centered cubic (FCC) metals, where it was shown that H can rearrange the surface dislocation network through stresses arising at the boundaries¹⁵. Such an observation of external-stress-free dislocation motion has not been reported in a BCC metal. This, at first glance, is not surprising: Compared to FCC, BCC H solubility is lower by orders of magnitude¹⁶. This is reported to have the effect of limiting H diffusion or segregation at the grain boundaries^{17,18}. Although not proven experimentally, it could be speculated that this would, in turn, significantly reduce the level of

¹Department of Materials Science and Engineering, MIT, Cambridge, MA, USA. ²Department of Nuclear Science and Engineering, MIT, Cambridge, MA, USA.

³These authors contributed equally: Kyung-Shik Kim, Qing-Jie Li. ✉ e-mail: tasan@mit.edu

H-induced local stresses at the boundaries—an important contributing factor in the H-induced dislocation motion in FCC metals¹⁵. It should be noted, however, that experiments on deuterium-charged martensitic steels showed that the H concentration can be higher at dislocation cores compared to grain boundaries¹⁹, and computational work of BCC crystals revealed the presence of attractive forces between embedded H (rather than a flux of H) and dislocations^{20–23}. These findings motivate the present study, since they suggest that the H-induced dislocation motion can be potentially realized, even when H is not diffusing or segregating at grain boundaries at comparable levels to the case of FCC metals. In this work, we demonstrate that dislocations in a BCC alloy can either be moved or pinned upon H charging, which is explained by the attractive dislocation–H flux interactions.

Results and discussion

Observations of hydrogen-induced dislocation motion

The alloy investigated in this study is a commercial 430 stainless steel (ASTM A240). The microstructure of this steel is ferritic (BCC), with random crystallographic texture as demonstrated by Supplementary Fig. 1. Various in-situ techniques are used in this study (Supplementary

Fig. 2). The in-situ H charging setup employed in the present study was designed to observe the dislocations through SEM-ECCI while electrochemically charging H (Supplementary Fig. 2a and b), allowing us to investigate dislocation response to H diffusion. In Fig. 1, backscattered electron (BSE) images reflect different stages of H diffusion in which the white features represent the dislocations²⁴, introduced to the system beforehand by uniaxial tension (1%).

These images reveal, at first glance, no difference in the surface dislocation network during H charging. Upon careful inspection, however, intriguingly, we could resolve dislocations moving small distances as H was diffusing through the sample, best seen in the provided movie files (Supplementary Video 1, Supplementary Video 2). Such dislocations are shown by the yellow arrows in Fig. 1a and e, for which higher magnification before-after views are provided in Fig. 1b, c and g. The length scales associated with these dislocation activities can be more easily seen using the gray value profiles provided in Fig. 1d and h. In rare cases, H charging induced disappearance of dislocations was also observed (see green arrows in Fig. 1e and f), suggesting out-of-plane dislocation motion. It should be noted, however, that only a small fraction of the dislocations (quantified below) could be detected to be

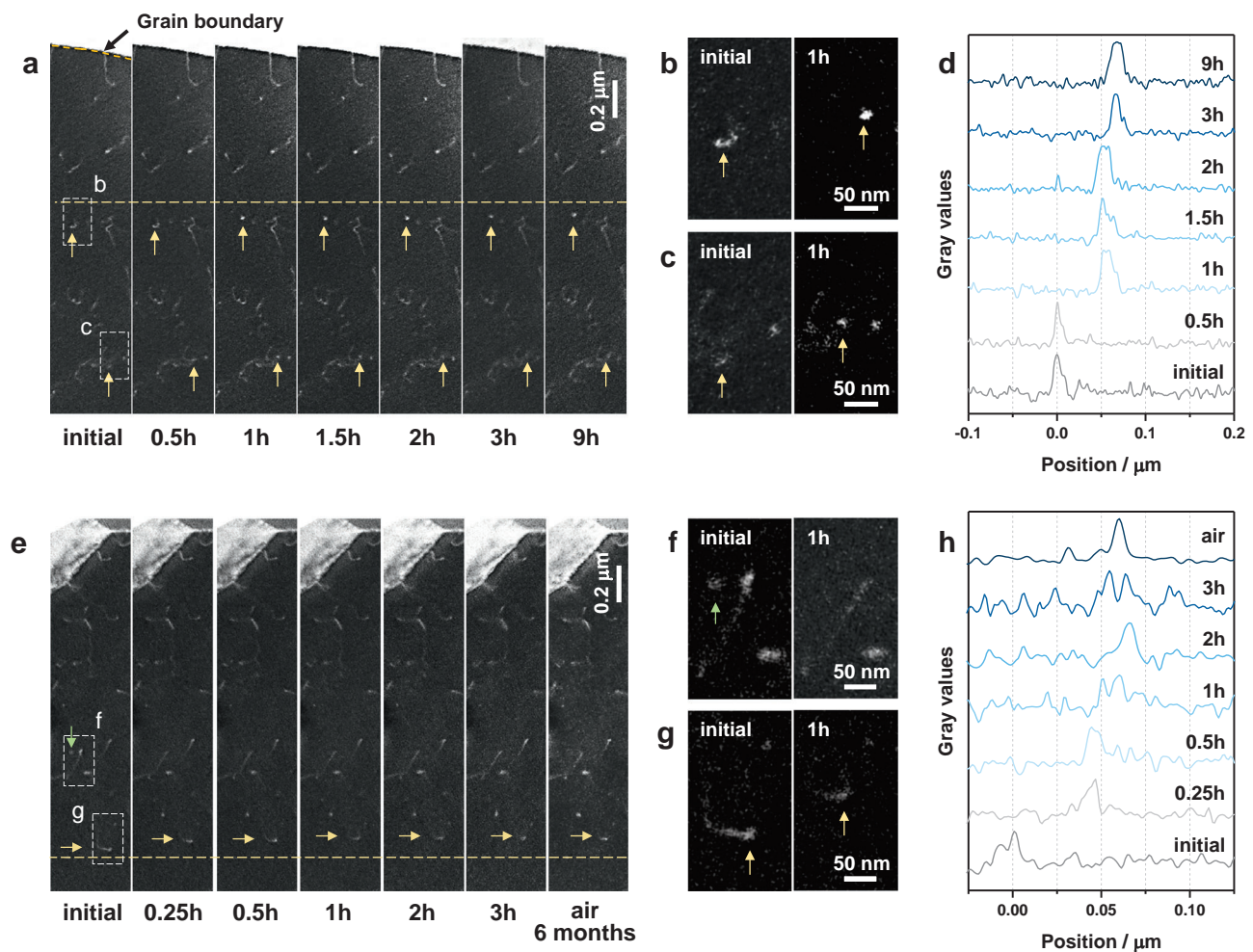


Fig. 1 | Dislocation motion during hydrogen charging observed with Electron Channeling Contrast Imaging (ECCI). **a** The ECCI analysis of dislocations as a function of the hydrogen charging time up to 9 h. **b**, **c** Magnified images of the area marked by dotted rectangles in **(a)**, showing before and after 1 h of hydrogen charging. **d** The pixel grayscale value plot showing the relative location of the dislocation in **(b)**. **e** The dislocation activity in another sample, during three hours of hydrogen charging followed by 6 months of air aging. **f**, **g** Magnified images of the area marked by dotted rectangles in **(e)**, showing before and after one hour of

hydrogen charging. **h** The relative location of the dislocation in **(g)**. Dotted yellow lines in **(a)**, **(e)** are reference lines manually placed near the mobile dislocation based on nearby grain boundaries, which remain stationary during hydrogen charging. They serve as guides to the eye to help visualize subtle dislocation motion across time-lapse images. Dislocations indicated by yellow arrows represent those in motion, while the green arrow denotes a dislocation disappearing from the surface. Note that the thicknesses of the samples for **(a)** and **(e)** are different.

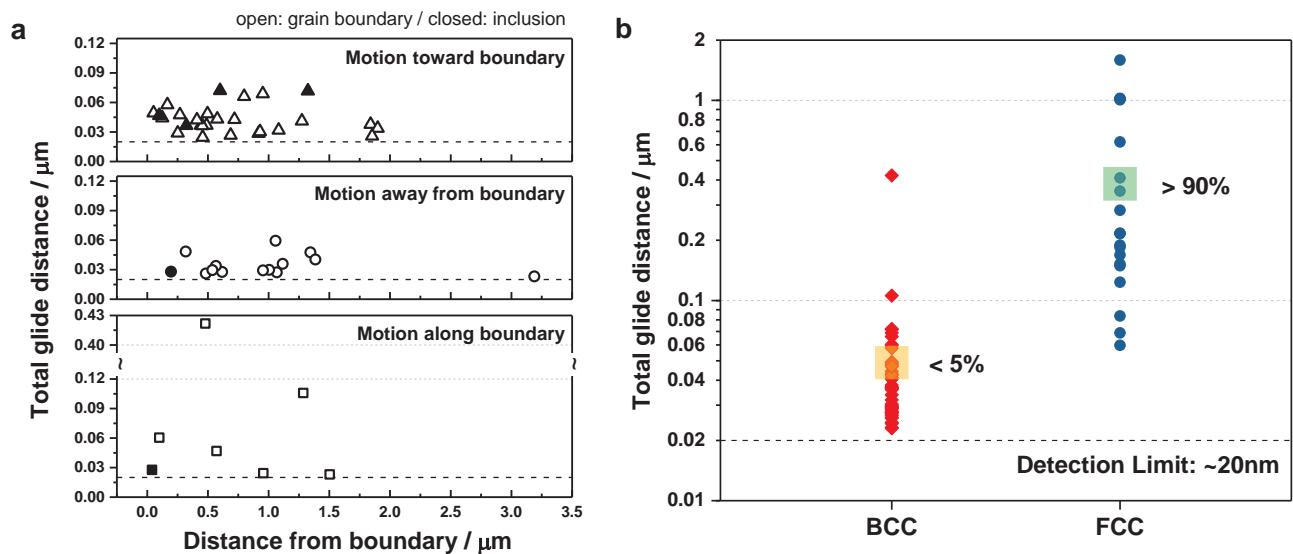


Fig. 2 | Microstructure effects on hydrogen-induced motion of dislocations. **a** The total glide distance of each observed dislocation with respect to their initial distance to the nearest boundary. **b** The comparison of the glide distance with the data of the previously studied FCC alloy¹⁵. Boxes colored in yellow and green for BCC and FCC, respectively, represent the average of the total motion distances. The

fraction of mobile dislocations for each case is indicated next to the boxes (calculated by comparing the length of the mobile dislocation segments to the total length of the dislocation network visible in the field of view). Dislocation activity below 20 nm was not considered in this analysis to avoid any data originating from image distortion. Source data is provided as a Source Data file.

moving upon H charging, while the majority of the dislocations in this BCC structure remained immobile (Supplementary Video 1, Supplementary Video 2). As a final confirmation, we carried out additional control experiments where we acquired BSE images under identical imaging conditions, but without H charging (Supplementary Fig. 3, Supplementary Video 3). Here in these experiments, all surface dislocations were stationary, confirming that H is responsible for the observed dislocation activity in Fig. 1.

The motion of dislocations in eight different grains (Supplementary Fig. 1c) was analyzed with respect to the distance from the adjacent boundaries, to assess if the previously-reported¹⁵ H segregation induced stress effect in FCC metals, plays also the key role here (Fig. 2a). The average distance moved by the studied dislocations is $49 \text{ nm} \pm 8 \text{ nm}$ (standard error of the mean), with 96% of the dislocations studied here exhibiting motions less than 75 nm. The data in Fig. 2a reveal that the dislocation activity has no distinct correlation to the distance to boundaries, since such an effect would have led to a clear trend of increased activity near boundaries. Since this analysis includes some experimental uncertainty (i.e., the glide planes are assumed to be parallel to the sample surface), we have carried out additional validation experiments. In-situ silver decoration test was conducted to investigate the diffusion and segregation of H by observing the formation of silver particles while charging H from the back surface (Supplementary Fig. 2a and e). The result also indicates (expectedly) that neither segregation of H at the grain boundaries nor its diffusion along them were prominent in this alloy, as silver particles were uniformly distributed throughout H charging (Supplementary Fig. 4a). Further comparisons with the previously-reported FCC case also indicate important differences. Out of all the distinguishable dislocation segments in all the grains investigated in the current study, only under 5% exhibited motion, while over 90% were shown to be moving in FCC¹⁵. Furthermore, the average distance of the dislocation motion in FCC is one order of magnitude larger than here (Fig. 2b). Altogether, the above results lead to the conclusion that the observed dislocation motion in BCC cannot be explained by H segregation at the boundaries.

To consider different mechanisms causing the observed dislocation activity, the data was closely inspected with respect to H charging

time. Electrochemical H permeation tests (schematically shown in Supplementary Fig. 2a and d) reveal that it takes ~15 min for H to penetrate through the sample thickness (Supplementary Fig. 4b). In-situ SEM experiments reveal, as best seen in Fig. 1d and h, that the major activity of the dislocations also initiate at these early stages, i.e., within 1 h from the start of the H charging. After this initial action, only limited dislocation motion is observed in all cases even up to 3 h of H charging (i.e., the point where the H flux is saturated based on the H permeation tests (Supplementary Fig. 4b)). No further dislocation activity was detected even after continuing the charging for up to 9 h (Fig. 1a, d). These observations suggest that there is a change in the H-induced effect in the later stages of charging, compared to initial stages. Interestingly, when the charged sample was exposed to air for 6 months, the dislocations stayed at their exact locations even though most H would have diffused out from the sample by that time (Fig. 1e, h).

Mechanisms of hydrogen-induced dislocation motion

To gain atomistic insights regarding the above observed H-induced dislocation activity in the BCC alloy, we carried out MD simulations on the interactions between H flux and a straight screw dislocation in BCC iron, using a recently developed embedded atom method (EAM) interatomic potential²⁵. Our choice of the EAM-based model system was mainly based on three criteria. First, the model system is expected to reproduce the compact and symmetrical screw dislocation core structure as predicted from density functional theory calculations²⁶. Second, the interactions between the screw dislocations and H should be accurately modeled. Finally, the H-H interactions in the bulk should also be correctly described, as these interactions are critical in an H flux simulation. The EAM potential developed by Wen et al.²⁵ satisfies all three criteria. For example, this EAM potential employed the parameterization of Fe by Ackland et al.²⁷ which correctly reproduced the compact core structure of screw dislocation. It also correctly reproduces the DFT results of the binding energy between the screw dislocation and H atom; as well as the H-H interactions in bulk lattice, demonstrating no (unphysical) clustering. Once validated for screw dislocation–H interactions in the Fe–Cr system, recently introduced angular-dependent

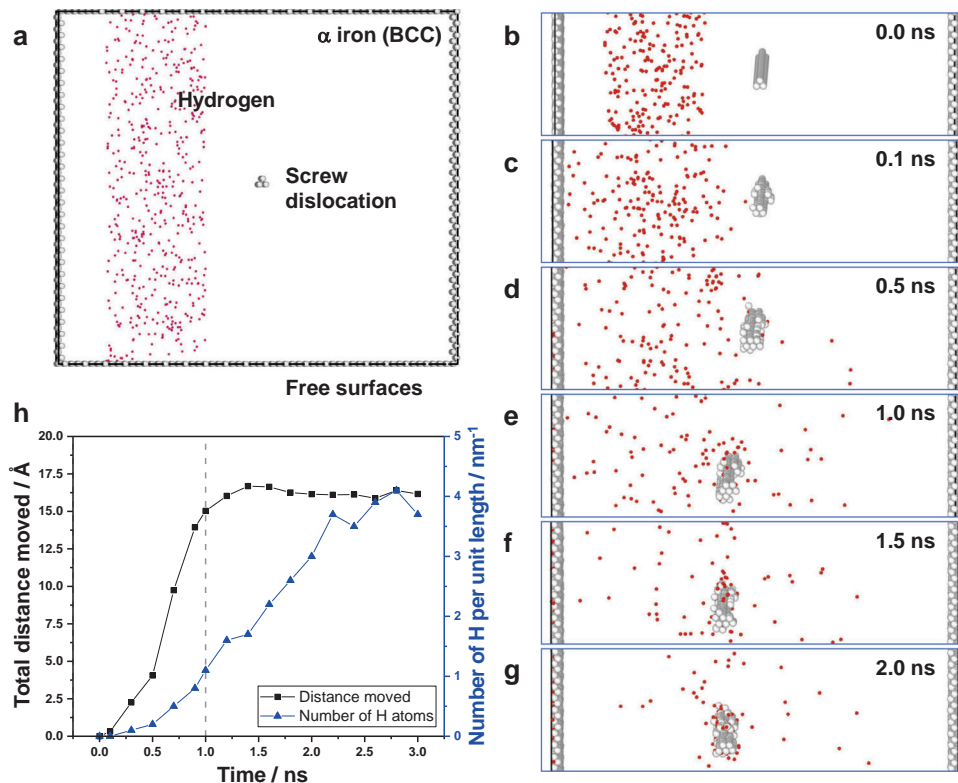


Fig. 3 | Hydrogen flux induced screw dislocation motion in BCC iron. a Initial configuration of the system. **b–g** The activity of the hydrogen atoms and the screw dislocation with respect of relaxation time. **h** The total distance of dislocation

motion (black square data points) and the number of H atoms per unit length of the screw dislocation (blue triangle data points), with respect to time. Note that dislocation length is 10 nm. Source data is provided as a Source Data file.

interatomic potentials (ADP) for FeCrH may also provide new insights in future work²⁸.

To comply with the samples in the experiments (with expectedly larger screw dislocation content upon 1% straining²⁹), a straight screw dislocation was introduced at the center of the simulation box (Fig. 3a). The dislocation density in the current MD simulation setup is $6 \times 10^{15} \text{ m}^{-2}$, which is one to two orders of magnitude higher compared to the experimental value (see Supplementary Information for details). That stated, our simulations were intended to simulate the local interactions between a screw dislocation and H flux, and free surface conditions were implemented (except in the $\langle 111 \rangle$ Burgers vector direction). The approach thus effectively excludes long-range elastic interactions between dislocations, enabling the study of an isolated dislocation. Next, a relatively high concentration of H atoms was introduced in the region neighboring the dislocation core, in the left half of the simulation box. The H concentration right before the dislocation–H interaction (-0.5 ns) is 0.16 at.%, or 1600 ppm, which is higher than that of the H concentration in typical experiments. The relatively high H concentration was intended to escalate the effects of H flux within a limited simulation time. Then the entire system was relaxed at a constant temperature (300 K) and zero external stress. As can be seen from Fig. 3b–g, upon equilibration, H atoms rapidly diffuse into surrounding regions, leading to collective interactions with the dislocation core (also shown in Supplementary Video 4). On the other hand, the introduced screw dislocation moves in the opposite direction of the H flux, instead of remaining stationary and acting as a H trapping site. However, as more and more H atoms aggregate into the core, the screw dislocation eventually stops moving and is pinned at a location a few nm away from its starting position. Figure 3h plots the dislocation core position as a function of simulation time, which shows these stages more clearly. Here, it can be seen

that although the density of H trapped in the core of the dislocation is steadily increasing, the distance moved shows two separate regimes: of motion (induced by H concentration gradient) and of pinning (induced by H decoration). Note that similar results have also been reproduced when the H concentration is lowered (i.e., down below ~ 200 ppm), ruling out a H concentration governed effect (Supplementary Fig. 5). Overall, these results demonstrate that MD simulations well-correlate with the experimental results, where dislocation moves as the H flux reaches the dislocations, and then the dislocations get pinned upon a longer exposure (Figs. 1 and 3).

The H concentration gradient induced dislocation motion (Fig. 3b–g) indicates an attractive interaction between H atoms and the dislocation core. To verify this assumption, we first mapped out the H–dislocation binding energy distribution around the dislocation core region (Fig. 4). Here, binding energy is simply defined as the potential energy difference between a bound configuration and an unbound configuration (dislocation and H atom are well separated); the more negative the binding energy is, the stronger the attractive interactions. We randomly sampled more than 1000 sites in the dislocation core region. Each binding site was introduced by four steps: 1) a H atom was first randomly inserted into the dislocation core region; 2) this initial binding configuration was optimized by energy minimization; 3) the optimized configuration was then equilibrated at 300 K for 1 ps; and 4) the equilibrated configuration was further optimized by a final energy minimization. Figure 4a shows the sampled binding energy distribution as a function of binding sites' in-plane positions (projecting along dislocation line direction) relative to the dislocation core. The binding energy distribution shows clear patterns originating from the dislocation core structure, i.e., only certain layers and equivalent crystal planes contain highly attractive binding sites. We further project the 2D distribution along the radial direction to obtain a 1D potential well

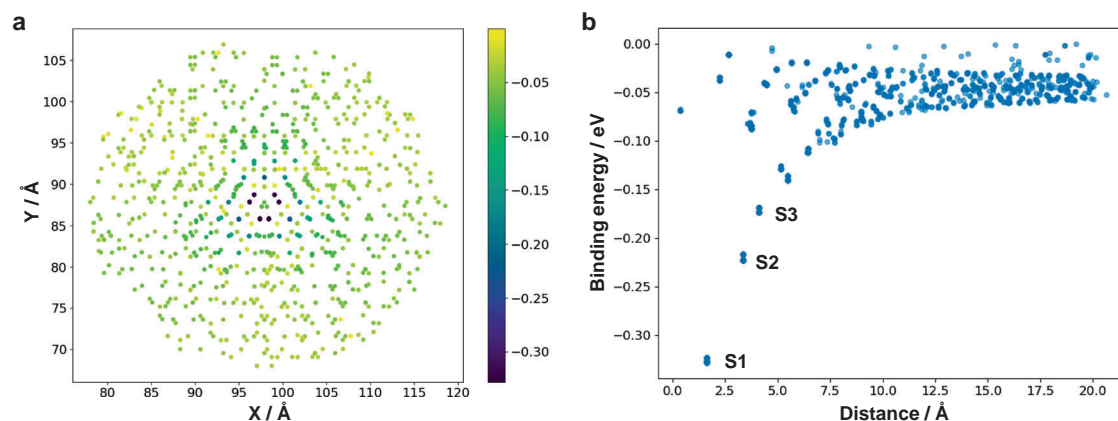


Fig. 4 | Distribution of binding energies between a straight screw dislocation and a hydrogen atom. **a** Binding energies as a function of hydrogen relative positions with respect to dislocation core. X is along $\langle 112 \rangle$ crystal direction, while Y is along $\langle 110 \rangle$ crystal direction. Color indicates the binding strength as marked on the color bar. **b** Binding energies as a function of hydrogen distance relative to

dislocation core. Three strong binding sites at short distances are marked as S1, S2, and S3. Binding energies are defined as the energy difference between bound configuration and unbound configuration (hydrogen and dislocation are well separated). Source data is provided as a Source Data file.

profile, see Fig. 4b. As can be seen, as a H atom approaches a dislocation core, there is a clear binding energy envelop showing discrete and increasingly more attractive interactions, as marked as S1, S2, S3, etc. The strongest binding energy reaches -0.3 eV, which is consistent with the value reported in ref. 25.

That stated, it requires collective interactions between a dislocation and many H atoms to induce observable motion of an extended dislocation segment. On the one hand, once H atoms enter the potential well as shown in Fig. 4b, they will be trapped into those discrete and strongly attractive binding sites, becoming less mobile. Such reduction in H mobility can help accumulate more H atoms in the discrete binding sites in both radial direction (such as S3, S2, and S1) and along the dislocation line, forming a favored H binding configuration (HBC) that collectively exerts an attractive force on the dislocation core. Note that the H-H interactions are weak²⁵ and multiple individual H-dislocation interactions can be approximated to be additive. On the other hand, the H concentration gradient enables a one-side HBC providing a biased driving force. When such biased HBC grows to sufficient density under the H flux, the collective attractive force can induce dislocation motion in the opposite direction of the H flux.

To further understand the driving forces provided by various HBCs, we carried out nudged elastic band (NEB) calculations to examine how HBCs affect the minimum energy paths (MEP) of motion for both free dislocation and locally pinned dislocation. Figure 5a and b shows how the MEP of a screw dislocation migration changes with increasing number of S2 H atoms in front of a free dislocation line. Our NEB calculations followed the procedure of previous work, where the correlated double-kink nucleation process was found to be more favored in experiments with low stress levels³⁰. As can be seen in Fig. 5a, when the number of S2 H atoms is increased from 0 to 5, the relative potential energy of final states is lowered from 0.00 eV to -0.55 eV, while the activation barrier is significantly reduced from 0.68 eV to 0.14 eV. This suggests: i) strong driving force of S2 HBCs to induce dislocation motion, and ii) accelerated kinetics even without any external stresses. Such result is also consistent with previous works showing H-induced decrease in the energy state and activation energy of the dislocation^{4,31,32}. We note that S2 H atoms need to be correlated to effectively lower the activation barrier, i.e., when the distance between two S2 H atoms is close to -10 nm, the activation barrier approaches that in the case of one S2 H atom (see the inset of Fig. 5a). Based on the calculated activation barriers, we can estimate the timescales on which the HBC-induced dislocation migration may

occur. The rate of double-kink nucleation can be written as $R = \nu \cdot \exp\left(\frac{-E_a}{k_B T}\right)$, where ν is the attempt frequency (on the order of 10^{11} s^{-1}), E_a is the activation energy, k_B is Boltzmann's constant, and T is temperature. The relevant timescale is proportional to the inverse of rate, i.e., $\tau \sim 1/R = \frac{1}{\nu} \exp\left(\frac{E_a}{k_B T}\right)$. At room temperature, with the assistance from zero to five S2 H atoms, the timescales for screw dislocation migrations are 10^0 s , 10^{-2} s , 10^{-3} s , 10^{-5} s , 10^{-7} s , and 10^{-9} s , respectively. We can see that even with one S2 H atom, the migration can occur on experimentally relevant timescale and be two orders of magnitude faster than that without S2 H atoms. Figure 5b shows representative intermediate configurations along the MEP for the case of two S2 H atoms, where the HBC induces a correlated double-kink nucleation followed by side migration of kinks that eventually propagates the dislocation to the next potential valley.

For locally pinned dislocations, our NEB calculations also suggest that S2 HBCs provide effective driving force to accelerate the migration and de-pinning. We found that when a screw dislocation is locally pinned (by three S1 H atoms in current calculations, Fig. 5d), double-kink nucleation often prefers to occur at locations a few nm away from the pinning location, rather than on the pinning site. This leads to similar MEP profiles as those for free dislocation, except for the pinch-off of pinning H atoms, see Fig. 5c and d. Again, the barrier for double-kink nucleation is significantly reduced with increasingly more S2 H atoms in front of the free segments. Meanwhile, the pinch-off process (the second hump on the top part of MEPs) seems not encountering a large barrier due to opposite kinks annihilation. Figure 5d shows a series of intermediate configurations along the MEP for the case of two S2 H atoms, demonstrating processes such as the correlated double-kink nucleation, side migration of kinks, and pinch-off of pinning H atoms. However, it should be noted that the number of S2 H atoms should be greater than that of pinning H atoms, for the newly migrated dislocation to be more energetically stable. Such NEB calculations further suggest that if there are more mobilizing H atoms than pinning H atoms, a dislocation segment tends to migrate, and the driving force is proportional to the number of net mobilizing H atoms. Also see Supplementary Fig. 6 for direct MD simulations on how biased HBCs induce the motion of a small dislocation segment.

The above NEB calculations and analyses lend support for HBC-induced dislocation motion on relevant experimental timescales. To further understand the HBC-induced dislocation motion distances on experimentally relevant length scale, we carried out coarse-grained

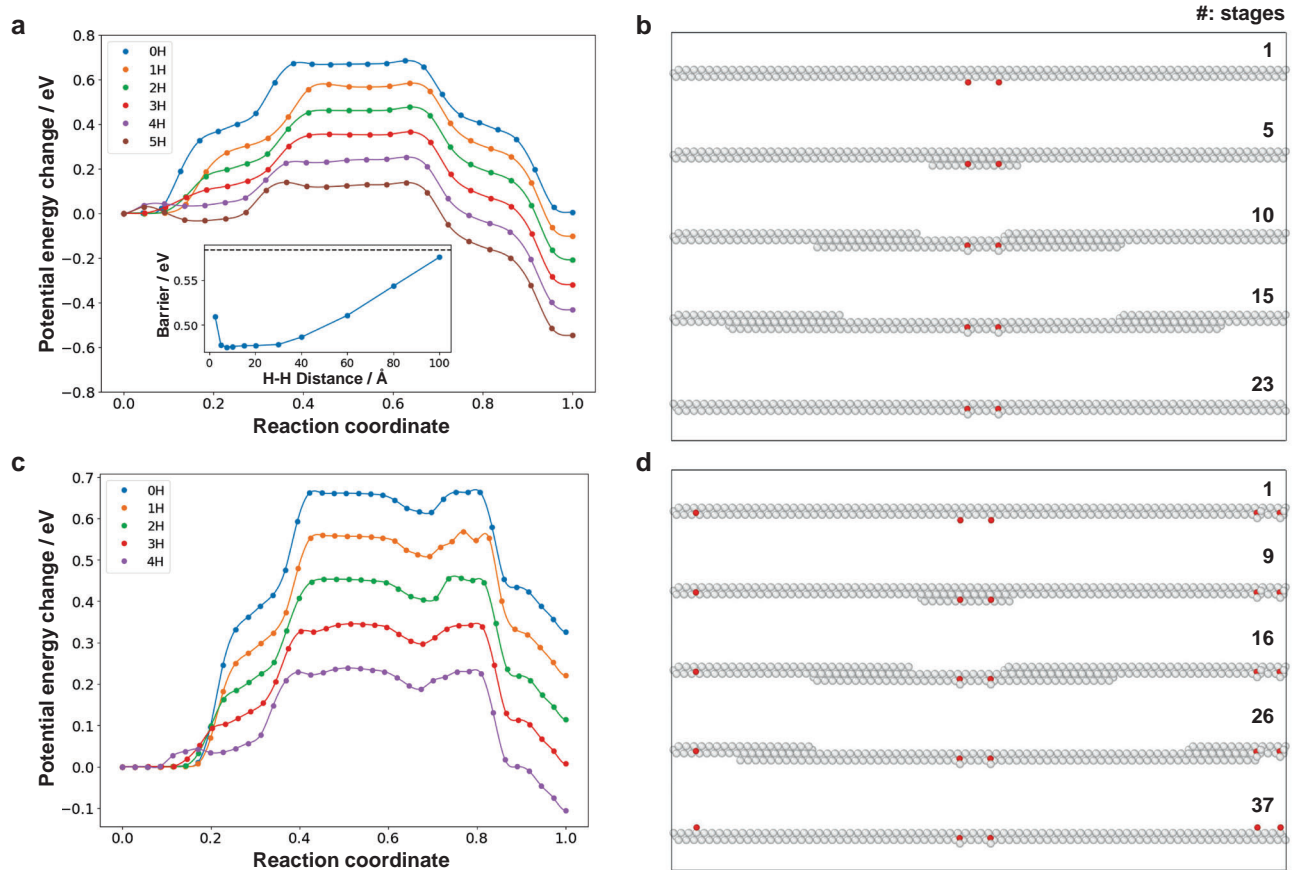


Fig. 5 | Effects of hydrogen binding configurations (HBCs) on the minimum energy pathway (MEP) of screw dislocation motion without external stress. **a** MEPs of screw dislocation motion with increasing number of S2 H atoms (see Fig. 4 for binding sites definition) in front of a free dislocation (from zero hydrogen atoms to five hydrogen atoms). Inset shows how the activation barrier changes when the distance between two S2 hydrogen atoms varies. **b** Representative

intermediate images along the MEP for the case of two S2 hydrogen atoms induced dislocation motion (green curve in **a**). **c** MEPs for locally pinned screw dislocation motion with various number of S2 hydrogen atoms in front of the dislocation line. **d** Intermediate configurations along the MEP for the case of two S2 hydrogen atoms in **(c)** (green curve). Hydrogen atoms are in red, while defect Fe atoms are in gray and perfect Fe atoms are not shown.

simulations by following simple rules: 1) H atoms diffuse in a random-walking manner; 2) a local dislocation segment migrates toward the potential valley with net mobilizing S2 H atoms counted within a cut-off distance; 3) if there is no S2 H atoms around, a local dislocation segment migrates to minimize the motion-direction-difference between itself and its neighbors (mimic line tension effects); and 4) kinks diffuse along free dislocation line in terms of random walk. In our simulation, we treat a long dislocation line as connected discrete units of 1 nm length. We first set a fixed number of H sources near surface (e.g., keeping a constant number of H atoms within the surface layers, usually a few nm) and then let H atoms naturally diffuse into bulk to create a H flux. During the H atoms diffusion process, once S2 H atoms are detected, we update the dislocation line morphology by rules 2) to 4), and then repeat such process until a certain maximum iteration is reached.

We tested two special cases to estimate a range of possible HBC-induced dislocation motion distances. In the first case, we assume H flux is normal to the dislocation line. To that end, a single H source near the surface was introduced to mimic a low concentration of H. A screw dislocation with a length of 500 nm was introduced 20 nm below the surface, for the sake of computational efficiency. When updating dislocation morphology, we chose a neighbor cut-off distance of 5 nm for counting S2 H atoms, and 10 nm for counting neighboring dislocation segments. For counting both S2 H atoms and dislocation segments, a linearly decaying weight factor was assigned to each neighbor, and the result is a weighted average over neighbors (see Supplementary Fig. 7

for a schematic illustration). Periodic boundary conditions were applied along dislocation line direction. With such a setup, we ran the simulation for a few hundreds of steps until there was no obvious evolution of dislocation morphology. It turns out, in such scenario, the dislocation motion distance is quite limited, usually on the order of a few nm (see Supplementary Video 5 for details).

In the second case, we assume the H flux has certain angle relative to the dislocation line direction. To achieve this, we only allow H atoms diffuse into a progressively increasing window from one end of the dislocation line, such that H atoms largely interact with dislocation segments in a sequential order (see Supplementary Fig. 8 for a schematic illustration). In this simulation, we used free surface in the dislocation line direction and increased the interacting window by 5 nm relative to the last pinned H atom at each step; all other settings were kept similar to the first case. One may tune the increment of interacting window to achieve the effects of different relative angles. In contrast to the outcome from the first case, the dislocation motion distance in the current case can be a few orders of magnitude longer and is largely limited by the H source supply and the initial dislocation line orientation. As can be seen in Supplementary Video 6, dislocation moved up to 30 nm after interacting with a few hundreds of H atoms (it can be even longer if we continue the simulation). We note that the above results should represent two extreme cases: one with random H-dislocation interactions and another with strongly correlated H-dislocation interactions, leading to two distinct dislocation motion distances. In reality, the H-dislocation interactions may fall somewhere

in between and may show a distribution of motion distance depending on the specific experimental conditions, as seen in our experiment (Fig. 2). The local variations in the experimental results (i.e., many dislocations not moving while few others moving (Fig. 2b)) can also be explained by the local nature of the gradients. When the flux is spatially not uniform due to local variations in the microstructure, neither will be the pinning forces^{33–36}.

A final point can be made regarding the role of gradients in the observed phenomena. Earlier investigations suggested that a surface H gradient can cause a high rate of dislocation generation³⁷. Here, such a meso-scale residual stress effect is not captured by the lattice strain measurements during H charging (Supplementary Fig. 2c). Lattice strain was calculated from the synchrotron XRD data by analyzing the distortion of the diffraction rings³⁸. As shown in Supplementary Fig. 9a, the initial lattice strain level was calculated to be under 0.05%. During the five hours of H charging, there is no change in the lattice strain, nor in the lattice parameter (Supplementary Fig. 9b and c), indicating minimal effects contributing to the observed H-induced motions. It can be argued that the resulting gradient during H desorption³⁹ should be similar to the one introduced during initial charging, and that some dislocation activity should thus be expected at that final stage. Intriguingly, this was not the case during the H desorption experiments (Fig. 1e, h). It should be remembered, however, that the important difference between the two cases is the fact that during desorption, dislocations are already decorated by trapped H, causing pinning. While the trapped H would escape eventually afterwards (H trapping energy is reported to be -0.21 to -0.37 eV for screw dislocation core in BCC iron⁴⁰), this relatively slower process can induce a lower H gradient compared to the case of the initial charging, and some H atoms would likely still remain trapped at dislocation cores³⁹.

In summary, our experiments and simulations clearly demonstrate that H flux alone can move or pin dislocations in BCC metals. The former reveals sudden jumps at the initial stages of charging, followed by a regime of limited activity afterwards. The latter reveals that in the initial stage of H dislocation interactions, when only a few H atoms reach the dislocation, the attractive force between H atoms and the dislocation core can pull the dislocation towards the opposite direction of the flux. In the later regime where the dislocations are fully decorated with H, no more motion could be observed due to the solute-drag effect^{5,41,42}. Overall, these observations and the corresponding explanations help improve our understanding of the fundamental processes occurring during H ingress into metals (or H desorption from metals) in the absence of external stresses. Since these distinct stages of mobility or pinning can exist even in the same microstructure (influenced by relevant local factors such as H gradient and concentration), significant care should be taken in studying these H-induced effects experimentally or computationally. Further studies are also called for to study how these regimes reported here would change upon variations in the state of the material system and the H flux characteristics.

Methods

Experimental procedure

In-situ SEM-ECCI. The 430 grade stainless steel plate was first cut into tensile specimens with gauge dimensions of 42 mm, 16 mm, and 0.6 mm for length, width, and thickness, respectively. The tensile samples were strained to 1% elongation with a tensile testing machine (INSTRON 5984) attached with an extensometer. The displacement rate was 1 mm min^{-1} , corresponding to the initial strain rate of $3.97 \times 10^{-4} \text{ s}^{-1}$. In-situ hydrogen charging experiment was conducted inside the SEM (TESCAN MIRA3) with a home-built setup¹⁴. After the setup was installed, the SEM chamber was cleaned with a plasma decontaminator (Evactron RPS) for 20 min to avoid any contamination during the SEM investigation. Before H charging, electron backscatter diffraction (EBSD) mapping was conducted on the area

of interest to measure the grain orientation. For H charging, aqueous solution of $30 \text{ g L}^{-1} \text{ NaCl} + 3 \text{ g L}^{-1} \text{ NH}_4\text{SCN}$ was used as the electrolyte and platinum wire as counter electrode. Current density of 5 A m^{-2} was applied for up to 9 h. ECCI images were taken every 15 to 30 min with accelerating voltage of 20 kV and working distance of 9 mm with a BSE detector. Both the charging and observing surfaces were first mechanically polished to 1200 grit sandpapers before the experiment, and the observing surface was additionally polished with colloidal silica for the quality of ECCI images. The final thickness of the samples was $500 \pm 100 \mu\text{m}$. All experiments were conducted at room temperature.

In-situ synchrotron XRD. High-energy X-ray diffraction experiments were conducted at the 11-ID-C beamline of Advanced Photon Source at Argonne National Laboratory with a home-built in-situ H charging setup⁴³. The beam energy was 105.7 keV with a sample-detector distance of 1.409 m. The beam size was $0.5 \times 0.5 \text{ mm}^2$. H was charged with the same conditions. During charging, X-ray diffraction patterns were recorded every 2 min. Each measurement was composed of 100 frames of 0.1 s exposure time. 1% pre-strained samples were also used, and the surfaces were mechanically polished with 1200 grit sandpapers. The final thickness of the samples was $500 \pm 100 \mu\text{m}$.

H permeation test. The permeation test was done with a modified Devanathan-Stachurski permeation cell according to the ISO 17081 standard, where two different cells were attached to each side of a sample⁴⁴. A circular area of 6.35 mm diameter was exposed on each side facing the charging and oxidizing cells. The charging condition in the charging cell was the same. The oxidation cell was filled with an aqueous solution of 0.1 M NaOH with platinum wire as the counter electrode and mercury/mercury oxide electrode as the reference electrode. $300 \text{ mV}_{\text{SCE}}$ was applied for the current detection. Both sides of the sample were mechanically polished with 1200 grit sandpapers. The final thickness of the permeation test sample was $400 \mu\text{m}$.

In-situ Ag decoration. H was charged to one surface of the sample, and silver solution was disposed on the opposite surface to perform in-situ Ag decoration experiment. The charging condition was also the same as in the other experiments, and aqueous solution of 4.3 mM $\text{KAg}(\text{CN})_2$ was used for the silver decoration. The sample surface was observed with an optical microscope through the transparent silver solution during hydrogen charging. Since the resolution of the optical microscope was limited, the 430 stainless steel was first aged at 1200°C for 30 min in an argon atmosphere to increase the grain size to $341 \pm 31 \mu\text{m}$. The sample was mechanically polished with 1200 grit sandpaper for the charging surface and with colloidal silica for the observing surface.

Simulations

Molecular dynamics simulations. In our MD simulations, a straight screw dislocation was introduced in the center of the simulation box of BCC iron single crystal surrounded by free surfaces. A high concentration of H atoms was randomly introduced in a region on the left of the dislocation. We expected these H atoms, upon MD relaxation, to diffuse toward the screw dislocation, leading to a H flux that interacts with the dislocation core. The screw dislocation was introduced according to the displacement field from anisotropic elasticity. H atoms were randomly introduced; but we kept all H atoms at least 1.25 \AA apart from existing Fe atoms. The interaction between H and Fe atoms is described by an EAM potential²⁵. This initial configuration was first optimized by energy minimization, after which the entire system was subjected to MD simulation at 300 K for 7 ns. Periodic boundary conditions were imposed along the dislocation line direction and free surfaces in the other two directions. Pressure (zero pressure along dislocation line direction) and temperature were controlled by the

Nose-Hoover thermostat/barostat. An integration time step of 1 fs was used for all simulations.

Nudged elastic band calculations. In our nudged elastic band (NEB) calculations, the initial minimum energy path (MEP) guess was generated following the procedure detailed in ref. 31, to include the correlated double-kink nucleation process. A spring constant of $1.0 \text{ eV } \text{Å}^{-2}$ was used for both parallel nudging force and perpendicular nudging force (to prevent kinked path). The saddle point was finally located by climbing image method⁴⁵. In all NEB calculations, we considered a 20 nm long $1/2 < 111 >$ screw dislocation gliding on $\{110\}$ plane. Periodic boundary conditions were applied in the dislocation line direction and free surfaces in the other two directions (both are 10 nm in length). All simulations were carried out using the LAMMPS package⁴⁶ and analyzed using the Ovito package⁴⁷.

Coarse-grained simulations. The coarse-grained simulation on H-induced dislocation motion was carried out by following rules: 1) H atoms diffuse in a random-walking manner; 2) a local dislocation segment migrates toward the potential valley with net mobilizing S2 H atoms counted within a cutoff distance in dislocation line direction; 3) if there is no S2 H atoms around, a local dislocation segment migrates to minimize the motion-direction-difference between itself and its neighbors (mimic line tension effects); and 4) kinks diffuse along free dislocation line in terms of random walk. A long dislocation line was treated as connected discrete units of 1 nm length. H flux was created by keeping a constant number of H atoms within the surface layers (usually a few nm) and the subsequent natural diffusion of H atoms into bulk. The dislocation line morphology was updated once S2 H atoms were detected, following rules 2) to 4). Such H-diffusion + dislocation morphology update cycle was repeated until a certain maximum iteration was reached. In updating dislocation morphology, we considered one segment unit at each time by 1) first calculating the weighted average position (along normal direction to dislocation line) for neighboring S2 H atoms and the segment moves toward the average normal position of S2 H atoms; and 2) if there is no S2 atoms, then the segment moves toward the direction pointing to the average normal position of neighboring segments, mimicking the effect of line tension. Weight factor was based on a linear decay from 1 to 0 when the location along dislocation line varies from current segment to a cutoff distance (5 nm for S2 H atoms and 10 nm for dislocation segments, respectively).

Data availability

The data generated in this study are available in the Supplementary Information and Source Data files. Atomic coordinates used in the simulations are accessible via the Materials Cloud repository <https://doi.org/10.24435/materialscloud:nt-5q>. Source data are provided with this paper.

Code availability

The atomistic simulations/calculations code LAMMPS used in this work is publicly available at <https://github.com/lammps/lammps>.

References

- Shih, D. S., Robertson, I. M. & Birnbaum, H. K. Hydrogen embrittlement of α titanium: in situ TEM studies. *Acta Metall.* **36**, 111–124 (1988).
- Ferreira, P. J., Robertson, I. M. & Birnbaum, H. K. Hydrogen effects on the interaction between dislocations. *Acta Mater.* **46**, 1749–1757 (1998).
- Huang, L. et al. Quantitative tests revealing hydrogen-enhanced dislocation motion in α -iron. *Nat. Mater.* **22**, 710–716 (2023).
- Wang, S., Hashimoto, N. & Ohnuki, S. Quantitative tests revealing hydrogen-enhanced dislocation motion in α -iron. *Sci. Rep.* **3**, 2760 (2013).
- Song, J. & Curtin, W. A. Mechanisms of hydrogen-enhanced localized plasticity: an atomistic study using α -Fe as a model system. *Acta Mater.* **68**, 61–69 (2014).
- Xie, D. et al. Hydrogenated vacancies lock dislocations in aluminium. *Nat. Commun.* **7**, 13341 (2016).
- Birnbaum, H. K. & Sofronis, P. Hydrogen-enhanced localized plasticity—a mechanism for hydrogen-related fracture. *Mater. Sci. Eng. A* **176**, 191–202 (1994).
- Beachem, C. D. A new model for hydrogen-assisted cracking (hydrogen “embrittlement”). *Metall. Trans.* **3**, 441–455 (1972).
- Troiano, A. R. The role of hydrogen and other interstitials in the mechanical behavior of metals (1959 Edward De Mille Campbell Memorial Lecture). *Metall. Microstruct. Anal.* **5**, 557–569 (2016).
- Oriani, R. A. Hydrogen embrittlement of steels. *Annu. Rev. Mater. Sci.* **8**, 327–357 (1978).
- Song, J. & Curtin, W. A. Atomic mechanism and prediction of hydrogen embrittlement in iron. *Nat. Mater.* **12**, 145–151 (2013).
- Nagumo, M. Function of hydrogen in embrittlement of high-strength steels. *ISIJ Int.* **41**, 590–598 (2001).
- Li, S. et al. The interaction of dislocations and hydrogen-vacancy complexes and its importance for deformation-induced proto nano-voids formation in α -Fe. *Int. J. Plast.* **74**, 175–191 (2015).
- Kim, J. & Tasan, C. C. Microstructural and micro-mechanical characterization during hydrogen charging: an in situ scanning electron microscopy study. *Int. J. Hydrog. Energy* **44**, 6333–6343 (2019).
- Koyama, M. et al. Origin of micrometer-scale dislocation motion during hydrogen desorption. *Sci. Adv.* **6**, eaaz1187 (2020).
- Da Silva, J. R. G. & Mclellan, R. B. The solubility of hydrogen in super-pure-iron single crystals. *J. Less Common Met.* **50**, 1–5 (1976).
- Lee, J.-Y. & Lee, S. M. Hydrogen trapping phenomena in metals with B.C.C. and F.C.C. crystals structures by the desorption thermal analysis technique. *Surf. Coat. Technol.* **28**, 301–314 (1986).
- Wei, F. G. & Tsuzaki, K. Hydrogen trapping phenomena in martensitic steels. Gaseous hydrogen embrittlement of materials in energy technologies. 493–525 (Woodhead Publishing, 2012).
- Chen, Y.-S. et al. Observation of hydrogen trapping at dislocations, grain boundaries, and precipitates. *Science* **367**, 171–175 (2020).
- Borges, P. P. O., Clouet, E. & Ventelon, L. Ab initio investigation of the screw dislocation-hydrogen interaction in bcc tungsten and iron. *Acta Mater.* **234**, 118048 (2022).
- Grigorev, P. et al. Interaction of hydrogen with dislocations in tungsten: an atomistic study. *J. Nucl. Mater.* **465**, 364–372 (2015).
- Bhatia, M. A., Groh, S. & Solanki, K. N. Atomic-scale investigation of point defects and hydrogen-solute atmospheres on the edge dislocation mobility in alpha iron. *J. Appl. Phys.* **116**, 064302 (2014).
- Lüthi, B., Ventelon, L., Rodney, D. & Willaime, F. Attractive interaction between interstitial solutes and screw dislocations in bcc iron from first principles. *Comput. Mater. Sci.* **148**, 21–26 (2018).
- Zaefferer, S. & Elhami, N.-N. Theory and application of electron channelling contrast imaging under controlled diffraction conditions. *Acta Mater.* **75**, 20–50 (2014).
- Wen, M. A new interatomic potential describing Fe-H and H-H interactions in bcc iron. *Comput. Mater. Sci.* **197**, 110640 (2021).
- Clouet, E., Bienvu, B., Dezerald, L. & Rodney, D. Screw dislocations in BCC transition metals: from ab initio modeling to yield criterion. *Comptes Rendus Phys.* **22**, 83–116 (2021).
- Ackland, G. J., Mendelev, M. I., Srolovitz, D. J., Han, S. & Barashev, A. V. Development of an interatomic potential for phosphorus impurities in α -iron. *J. Phys. Condens. Matter* **16**, S2629–S2642 (2004).
- Starikov, S. et al. Angular-dependent interatomic potential for large-scale atomistic simulation of the Fe-Cr-H ternary system. *Phys. Rev. Mater.* **6**, 043604 (2022).
- Okada, K., Shibata, A., Gong, W. & Tsuji, N. Effect of hydrogen on evolution of deformation microstructure in low-carbon steel with ferrite microstructure. *Acta Mater.* **225**, 117549 (2022).

30. Gordon, P. A., Neeraj, T., Li, Y. & Li, J. Screw dislocation mobility in BCC metals: the role of the compact core on double-kink nucleation. *Model. Simul. Mater. Sci. Eng.* **18**, 085008 (2010).
31. Barnoush, A. & Vehoff, H. Recent developments in the study of hydrogen embrittlement: Hydrogen effect on dislocation nucleation. *Acta Mater.* **58**, 5274–5285 (2010).
32. Wen, M., Fukuyama, S. & Yokogawa, K. Atomistic simulations of effect of hydrogen on kink-pair energetics of screw dislocations in bcc iron. *Acta Mater.* **51**, 1767–1773 (2003).
33. Díaz, A., Alegre, J. M. & Cuesta, I. I. A review on diffusion modelling in hydrogen related failures of metals. *Eng. Fail. Anal.* **66**, 577–595 (2016).
34. Pan, H., He, Y. & Zhang, X. Interactions between dislocations and boundaries during deformation. *Materials* **14**, 1012 (2012).
35. Tang, M., Cai, W., Xu, G. & Bulatov, V. V. A hybrid method for computing forces on curved dislocations intersecting free surfaces in three-dimensional dislocation dynamics. *Model. Simul. Mater. Sci. Eng.* **14**, 1139 (2006).
36. Rhee, M., Zbib, H. M., Hirth, J. P., Huang, H. & de la Rubia, T. Models for long-/short-range interactions and cross slip in 3D dislocation simulation of BCC single crystals. *Model. Simul. Mater. Sci. Eng.* **6**, 467 (1998).
37. Armacani, M. E. & Oriani, R. A. Plastic deformation in B.C.C. alloys induced by hydrogen concentration gradients. *Mater. Sci. Eng.* **91**, 143–152 (1987).
38. Ott, R. T. et al. Micromechanics of deformation of metallic-glass-matrix composites from in situ synchrotron strain measurements and finite element modeling. *Acta Mater.* **53**, 1883–1893 (2005).
39. Jiang, D. E. & Carter, E. A. Diffusion of interstitial hydrogen into and through bcc Fe from first principles. *Phys. Rev. B* **70**, 064102 (2004).
40. Kholobina, A. S. et al. Hydrogen trapping in bcc iron. *Materials* **13**, 2288 (2020).
41. Cottrell, A. H. & Dexter, D. L. Dislocations and plastic flow in crystals. *Am. J. Phys.* **22**, 242–243 (1954).
42. Hu, S. Y., Li, Y. L., Zheng, Y. X. & Chen, L. Q. Effect of solutes on dislocation motion—a phase-field simulation. *Int. J. Plast.* **20**, 403–425 (2004).
43. Kim, J., Kang, J. & Tasan, C. C. Hydride formation in Ti6Al4V: an in situ synchrotron X-ray diffraction study. *Scr. Mater.* **193**, 12–16 (2021).
44. ISO, ISO 17081: Method of measurement of hydrogen permeation and determination of hydrogen uptake and transport in metals by an electrochemical technique <https://www.iso.org/standard/64514.html> (2004).
45. Henkelman, G., Uberuaga, B. P. & Jónsson, H. A climbing image nudged elastic band method for finding saddle points and minimum energy paths. *J. Chem. Phys.* **113**, 9901–9904 (2000).
46. Thompson, A. P. et al. LAMMPS—a flexible simulation tool for particle-based materials modeling at the atomic, meso, and continuum scales. *Scr. Mater.* **238**, 115755 (2024).
47. Stukowski, A. Visualization and analysis of atomistic simulation data with OVITO—the Open Visualization Tool. *Model. Simul. Mater. Sci. Eng.* **18**, 015012 (2010).

Acknowledgements

The authors acknowledge financial support by U.S. Department of Energy, Office of Energy Efficiency & Renewable Energy (EERE) under Award No. DE-EE0008830. In-situ synchrotron H charging tests were conducted at beamline 11-ID-C of the Advanced Photon Source, Argonne National Laboratory, USA.

Author contributions

C.C.T. conceptualized and supervised the project; K.-S.K. designed the project and performed experiments; Q.-J.L. performed the simulations under the guidance of J.L.; K.-S.K. and Q.-J.L. prepared the first draft, and all authors contributed to discussions and revision of the manuscript.

Competing interests

The authors declare no competing interests.

Additional information

Supplementary information The online version contains supplementary material available at <https://doi.org/10.1038/s41467-025-59314-z>.

Correspondence and requests for materials should be addressed to Cemal Cem Tasan.

Peer review information *Nature Communications* thanks Alexander Bakaev, Mitsuhiro Itakura and the other, anonymous, reviewer(s) for their contribution to the peer review of this work. A peer review file is available.

Reprints and permissions information is available at <http://www.nature.com/reprints>

Publisher's note Springer Nature remains neutral with regard to jurisdictional claims in published maps and institutional affiliations.

Open Access This article is licensed under a Creative Commons Attribution-NonCommercial-NoDerivatives 4.0 International License, which permits any non-commercial use, sharing, distribution and reproduction in any medium or format, as long as you give appropriate credit to the original author(s) and the source, provide a link to the Creative Commons licence, and indicate if you modified the licensed material. You do not have permission under this licence to share adapted material derived from this article or parts of it. The images or other third party material in this article are included in the article's Creative Commons licence, unless indicated otherwise in a credit line to the material. If material is not included in the article's Creative Commons licence and your intended use is not permitted by statutory regulation or exceeds the permitted use, you will need to obtain permission directly from the copyright holder. To view a copy of this licence, visit <http://creativecommons.org/licenses/by-nc-nd/4.0/>.

© The Author(s) 2025